

# Experimental and numerical investigation of single-phase heat transfer using a hybrid jet-impingement/micro-channel cooling scheme

Myung Ki Sung, Issam Mudawar \*

*Boiling and Two-Phase Flow Laboratory, School of Mechanical Engineering, Purdue University, 585 Purdue Mall, West Lafayette, IN 47907, USA*

Received 29 April 2005; received in revised form 17 August 2005

Available online 18 October 2005

## Abstract

Experimental and numerical methods were used to explore the cooling performance of a new hybrid device consisting of a slot jet impinging into a micro-channel, thus capitalizing upon the merits of both cooling configurations. The three-dimensional heat transfer characteristics of this device were analyzed using the standard  $k-\epsilon$  turbulent model. Numerical predictions for liquid PF-5052 show excellent agreement with experimental measurements. Vorticity effects are shown to greatly influence cooling performance outside the impingement zone. Higher jet Reynolds numbers yielded stronger attachment to the heated surface and lower surface temperatures. The model was also used to optimize the cooling performance for a water-cooled device. Lower surface temperatures were achieved by decreasing jet width and micro-channel height. These findings are used to recommend a simplified hybrid cooling geometry in pursuit of both lower surface temperatures and smaller temperature gradients across the heated surface.

© 2005 Elsevier Ltd. All rights reserved.

## 1. Introduction

Many cooling schemes have been examined in recent years in pursuit of thermal solutions to the problem of heat flux escalation from electronic devices. Of these cooling schemes, jet-impingement and micro-channel flow are considered the two most effective solutions for devices demanding very high-flux removal, such as high-performance microprocessors, laser diode arrays, radars and X-ray anodes [1].

### 1.1. Jet-impingement cooling

Using a dielectric liquid, jet-impingement produces very large heat transfer coefficients in the impingement zone [2]. The abrupt reduction in cooling effectiveness away from the impingement zone can yield large temperature variations along the surface of the heat-dissipating device [3]. This problem can be circumvented by using an array of

jets, creating multiple, closely-spaced impingement zones. Earlier efforts provided valuable insight into the effects of coolant thermophysical properties [4] and interference between jets in multi-jet arrays [5]. In their literature survey, Downs and James [6] discussed how the use of multiple jets to enhance both heat removal and surface temperature uniformity, can be marred by jet interference effects. Interference between circular jets has been shown to reduce heat transfer and produce complex spatial variations in the heat transfer coefficient because of eddy formation and boundary layer separation, as revealed in the flow visualization studies by Goldstein and Timmer [7]. Another drawback to using multiple jets to cool a device surface is flow blockage between jets, especially for jets situated towards the center of the device surface, which complicates flow distribution and exit of the spent fluid [2]. Clearly, better means are needed to capitalize upon the merits of multiple jet impingement while facilitating better flow distribution inside of, and exit from, a cooling module.

Numerical methods have been used extensively to model jet-impingement fluid flow and heat transfer using a variety of turbulence models. Craft et al. [8] tested four different

\* Corresponding author. Tel.: +1 765 494 5705; fax: +1 765 494 0539.  
E-mail address: [mudawar@ecn.purdue.edu](mailto:mudawar@ecn.purdue.edu) (I. Mudawar).

**Nomenclature**

$A_{\text{jet}}$	area of jet	$T_{\text{in}}$	fluid inlet temperature
$A_t$	area copper block's top test surface	$u$	velocity component in $x$ direction
$C_{\mu}, C_1, C_2$	turbulence model constants	$U_i$	velocity vector
$c_p$	specific heat at constant pressure	$v$	velocity component in $y$ direction
$d_h$	hydraulic diameter of jet, $2W_{\text{jet}}$	$\dot{V}$	volume flow rate
$G$	production of turbulent energy	$w$	velocity component in $z$ direction
$H$	height of unit cell	$w_{\text{in}}$	fluid inlet velocity
$H_{\text{ch}}$	height of channel	$W$	width of unit cell
$H_{\text{gap}}$	height of side channels	$W_{\text{ch}}$	width of channel
$H_{\text{jet}}$	height of jet	$W_{\text{jet}}$	width of jet
$H_{\text{th}}$	height from unit cell bottom boundary to thermocouple holes	$W_w$	half-width of wall separating channels
$H_w$	height from unit cell bottom boundary to test surface	$x$	Cartesian coordinate
$k$	thermal conductivity; turbulent kinetic energy	$y$	Cartesian coordinate
$l$	iteration number	$y^+$	dimensionless distance normal to wall
$L$	length of unit cell	$z$	Cartesian coordinate
$L_{\text{jet}}$	length of jet		
$L_{\text{out}}$	distance between jet and channel outlet	<i>Greek symbols</i>	
$L_1, L_2, L_3$	distance between thermocouple holes	$\varepsilon$	dissipation rate of turbulent kinetic energy
$\dot{m}$	mass flux flow rate	$\mu$	dynamic viscosity
$n$	outer normal coordinate at interface between solid and liquid	$\mu_l$	eddy viscosity
$N$	number of jets in flow distribution plate	$\rho$	density
$Nu$	Nusselt number	$\sigma_k, \sigma_\varepsilon$	empirical constants in $k$ and $\varepsilon$ transport equations
$P$	pressure	$\omega$	specific dissipation rate of turbulent kinetic energy
$Pr$	Prandtl number		
$Pr_t$	turbulent Prandtl number	<i>Subscripts</i>	
$P_w$	electrical power supplied to copper block	av	average
$q'$	heat flux	f	fluid
$q''_{\text{eff}}$	effective heat flux based on top test surface area of copper block	in	inlet
$Re$	Reynolds number	out	outlet
$T$	temperature	s	solid
		t	turbulent
		$\Gamma$	interface between solid and liquid

turbulence models against experimental jet-impingement data. Park et al. [9] examined confined impinging slot jets with the  $k-\omega$  turbulence model. Baydar and Ozmen [10] investigated confined high Reynolds number impinging air jets using the standard  $k-\varepsilon$  turbulence model. They concluded that the  $k-\varepsilon$  model is capable of accurately predicting the flow characteristics.

### 1.2. Micro-channel cooling

Micro-channel heat sinks can yield heat removal rates comparable to those of jet-impingement schemes using far smaller coolant flow rates and more compact cooling hardware. Two of their drawbacks are large temperature rise along the direction of fluid flow and relatively high pressure drop [1]. Tuckerman and Pease [11] pioneered the use of micro-channel heat sinks for chip cooling. Their

heat sink was fabricated by chemically etching parallel micro-channels into a  $1.0 \times 1.0 \text{ cm}^2$  silicon wafer. Their heat sink yielded heat fluxes as high as  $790 \text{ W/cm}^2$  using water as working fluid. However, this outstanding performance was realized with enormous penalties in both pressure drop and temperature rise along the direction of fluid flow.

Several numerical studies have been published on the fluid flow and heat transfer characteristics of single-phase micro-channel heat sinks. Weisberg et al. [12] presented a two-dimensional model of micro-channel heat sinks by assuming both hydrodynamically and thermally fully developed flow. Fedorov and Viskanta [13] developed a three-dimensional model to account for development of both the velocity and temperature fields along the flow direction. Qu and Mudawar [14] investigated the transport characteristics of a micro-channel heat sink both experimentally and

numerically. They concluded the conventional Navier–Stokes and energy equations accurately predict the heat transfer characteristics of micro-channel heat sinks. Kim and Kim [15] presented analytical solutions for velocity and temperature distributions through micro-channel heat sinks based on the modified Darcy model for fluid flow and the two-equation model for heat transfer. Ng and Tan [16] performed three-dimensional numerical simulations of developing pressure-driven liquid flow in a micro-channel with an electric double layer effect. By combining the three-dimensional Poisson–Boltzmann equation and the Navier–Stokes equation, they calculated both the flow entrance length and Nusselt number in the entry region. Ambatipudi and Rahman [17] performed numerical simulations of conjugate heat transfer in micro-channels using the finite-difference method with the SIMPLEST algorithm. They concluded that the Nusselt number can be increased by increasing channel depth. Furthermore, increasing the number of channels increased the local Nusselt number along the entire length of the channel.

The primary purpose of the present study is to capitalize upon the merits of both jet-impingement and micro-channel flow while minimizing the aforementioned drawbacks. A new hybrid jet-impingement/micro-channel flow configuration is examined in pursuit of better surface temperature uniformity during high-flux dissipation. This hybrid configuration is examined both experimentally and numerically. The experimental results are compared to predictions of a numerical model of the hybrid configuration. The numerical model is used to predict local and average

surface temperatures and to optimize the geometry of the hybrid cooling system.

## 2. Experimental apparatus

### 2.1. Flow loop

Fig. 1 shows a schematic diagram of the flow loop that was constructed to supply Fluorinert PF-5052 liquid to a test module housing the hybrid cooling device. Liquid from a reservoir was circulated in the flow loop by a centrifugal magnetic drive pump. The liquid first passed through a 5  $\mu\text{m}$  filter to prevent any solid particles from blocking the flow passages of the test module. Exiting the filter, the liquid was routed into one of two parallel rotameters for volume flow rate measurement. The liquid then entered an air-cooled finned-tube heat exchanger that cooled the liquid to the desired module inlet temperature. The liquid then entered the test module, which was fitted with throttling valves both upstream and downstream, before returning to a reservoir situated atop the aforementioned reservoir. The liquid drained by gravity to the lower reservoir.

### 2.2. Test module

As illustrated in Fig. 2(a), the test module consisted of a heater block, a flow distribution plate, a spacer, a cover plate, and 16 cartridge heaters. Fig. 2(b) shows a cross-sectional diagram of the test module with key dimensions. The

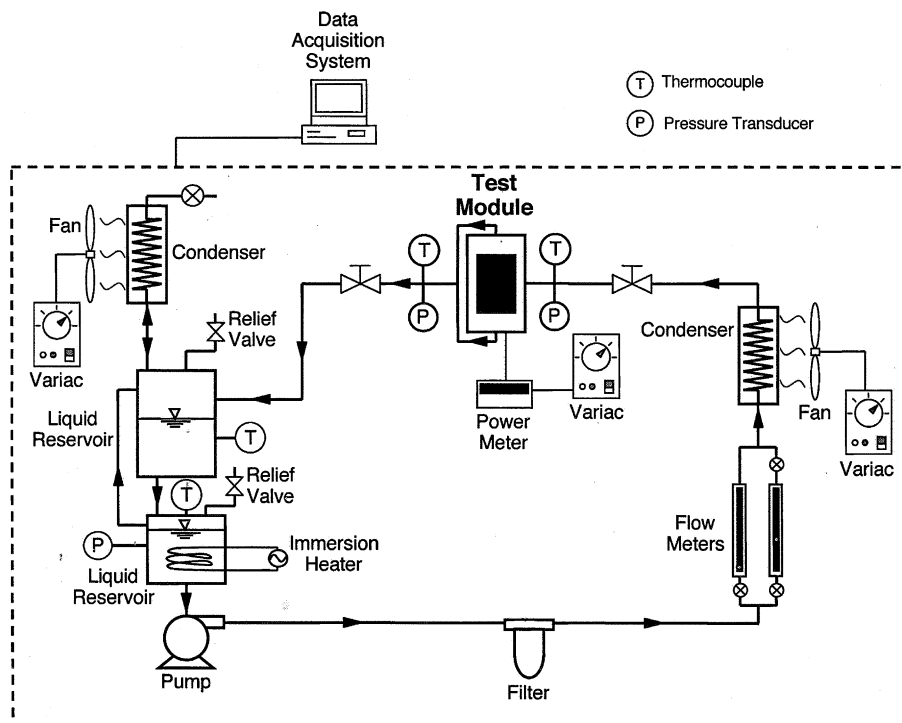


Fig. 1. Schematic of flow loop.

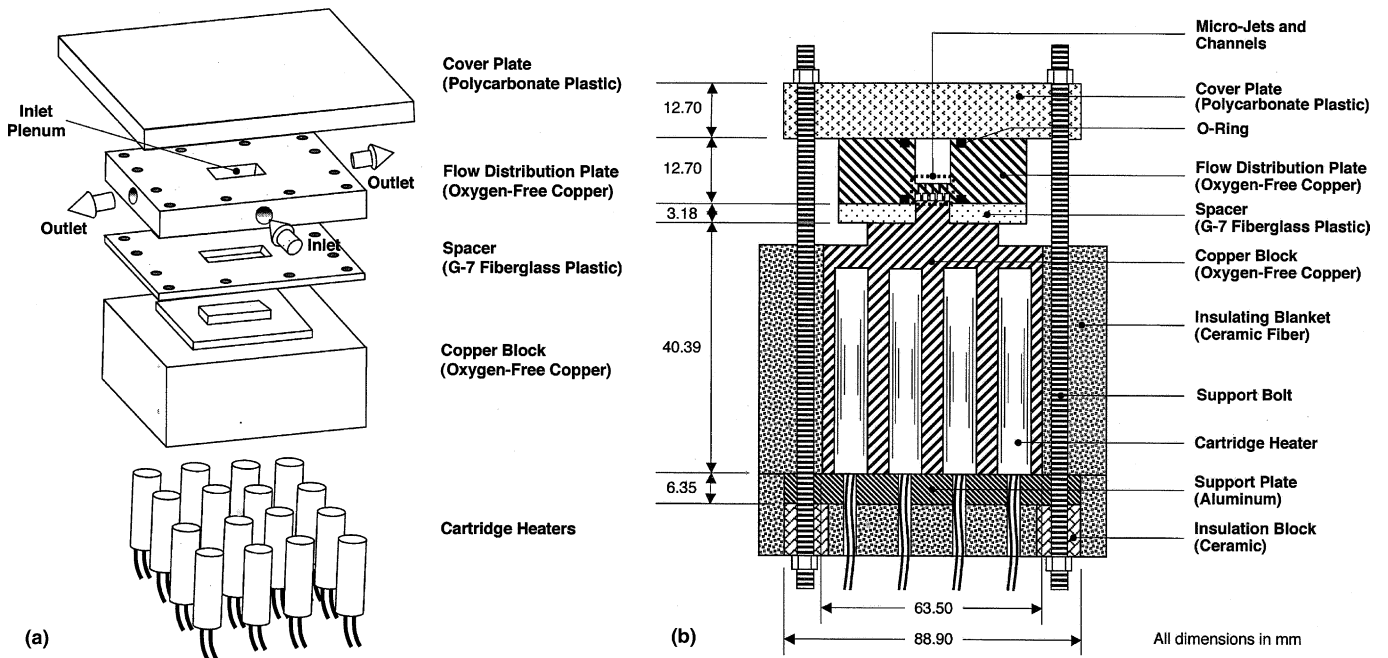


Fig. 2. (a) Test module construction. (b) Cross-section of module assembly.

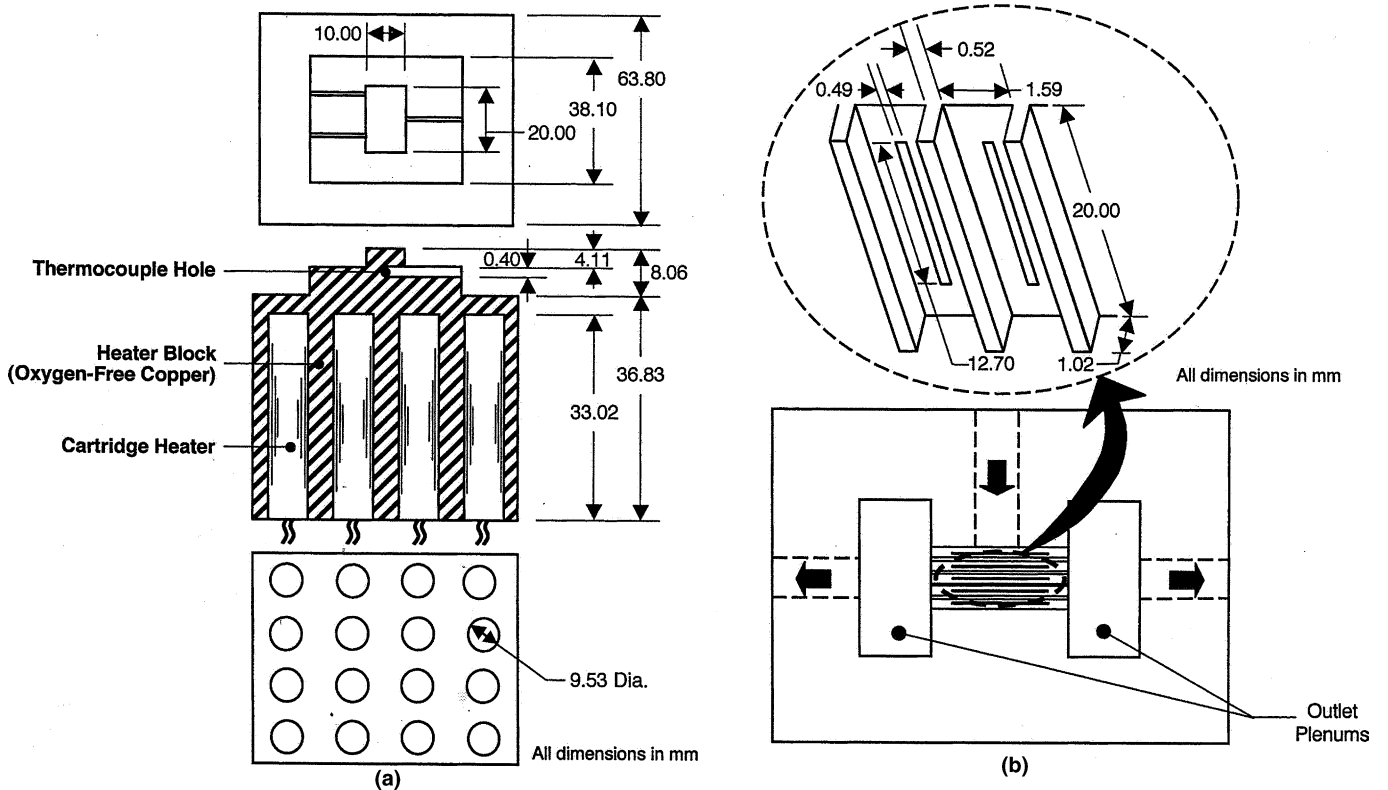


Fig. 3. Details of (a) heater block and (b) underside of flow distribution plate.

heater block was machined from a single block of oxygen-free copper that had an upper test surface area (exposed to the liquid flow) of  $1.0 \times 2.0 \text{ cm}^2$  as illustrated in Fig. 3(a). The block was tapered at the top in two steps to help ensure uniform temperature along the test surface. Three

chromel–alumel (K-type) thermocouples were inserted below the test surface. One was placed below the center of the test surface while the other two were situated along the flow direction to monitor spatial temperature changes along the surface. Sixteen holes were drilled into the

underside of the heater block to accommodate the cartridge heaters. The cartridge heaters were connected in a parallel/ series circuit and powered by a single 0–110 VAC variac. The power dissipation from the cartridge heaters was measured by a wattmeter. A spacer fabricated from high temperature fiberglass plastic surrounded the neck of the heater block leading to the test surface. This spacer as well as blanket insulation around the circumference and solid ceramic insulation at the bottom of the block helped minimize heat loss to the ambient. RTV silicone rubber was applied along the interface between the spacer and the heater block to prevent liquid leakage.

All geometrical details of the hybrid cooling configuration were machined into the flow distribution plate. This plate was fabricated from oxygen-free copper. As shown in Fig. 3(b), five parallel 1.59 mm wide by 1.02 mm deep channels were machined into the underside of the flow distribution plate, equidistantly spaced within a 1 cm width facing the test surface of the heater block. Five 0.48 mm wide, 0.76 mm deep, and 12.7 mm long slot jets were machined between the inlet plenum and the rectangular channels. The flow distribution plate contained one upstream plenum, covered atop with a polycarbonate plastic (Lexan) plate, and two downstream plenums. O-rings were used to prevent liquid leakage between the flow distribution plate and both the cover plate and the spacer.

### 2.3. Data acquisition

A Yamaha WT 2000 wattmeter was used to measure total power input to the 16 cartridge heaters. Readings from the heater and loop thermocouples and pressure transducers were recorded by an HP 3497A data acquisition system. The mean heat flux,  $q''_{\text{eff}}$ , from the test surface area of the heater block was calculated by dividing the electric power supplied to the cartridge heaters by the area of the test surface,  $A_t = 1.0 \times 2.0 \text{ cm}^2$ .

$$q''_{\text{eff}} = \frac{P_w}{A_t}. \quad (1)$$

Data were obtained at  $q''_{\text{eff}} = 36.96 \text{ W/cm}^2$  for a Reynolds number of  $Re = 1287$  and  $q''_{\text{eff}} = 46.07 \text{ W/cm}^2$  for  $Re = 5012$ , where the Reynolds number is based on jet inlet velocity and hydraulic diameter.

$$Re = \frac{\rho_f w_{\text{in}} d_h}{\mu_{f,\text{in}}}, \quad (2)$$

where  $d_h = 2W_{\text{jet}}$ ,  $w_{\text{in}}$  is the jet inlet velocity,

$$w_{\text{in}} = \frac{\dot{V}}{NA_{\text{jet}}}, \quad (3)$$

and  $\mu_{f,\text{in}}$  is based on the measured inlet temperature.

### 2.4. Measurement uncertainty

The heat loss was estimated at less than 5% of the total heat input. Uncertainties in the pressure transducer, rota-

meter, wattmeter, and thermocouple measurements were 0.5%, 1.0%, 0.5%, and 0.3 °C, respectively.

### 3. Numerical model

A three-dimensional model of the hybrid cooling scheme was constructed for comparison with the measured results. The same model was used to explore parametric trends of the local and average heat transfer characteristics in pursuit of optimal geometry for the hybrid cooling scheme.

A unit cell containing a single jet, a single channel and surrounding solid was used to perform the numerical analysis. Taking advantage of symmetry, the computational domain consisted of only one quarter of the unit cell. Fig. 4 illustrates the unit cell and corresponding coordinate system and key notations. Dimensions of the unit cell are given in Table 1.

The standard two-equation  $k$ - $\varepsilon$  turbulent model [18] was used to predict three-dimensional flow profiles and heat transfer characteristics of the computational domain. A staggered grid [19] was used to prevent non-physical results. Solid–liquid interfaces are governed by continuities of both temperature and heat flux,

$$T_{s,r} = T_{f,r} \quad (4)$$

and

$$-k_s \left. \frac{\partial T_s}{\partial n} \right|_r = -k_f \left. \frac{\partial T_f}{\partial n} \right|_r. \quad (5)$$

The governing equations were written in Cartesian tensor notation for steady, turbulent and incompressible flow with constant properties. For the fluid region, the continuity, momentum, and energy equations are expressed, respectively, as

$$\frac{\partial U_i}{\partial x_i} = 0, \quad (6)$$

$$\rho_f U_j \frac{\partial U_i}{\partial x_j} = -\frac{\partial P}{\partial x_i} + \frac{\partial}{\partial x_j} \left( (\mu_f + \mu_t) \frac{\partial U_i}{\partial x_j} \right), \quad (7)$$

and

$$\rho_f c_{p,f} U_j \frac{\partial T}{\partial x_j} = \frac{\partial}{\partial x_j} \left( \left( k_f + \frac{c_{p,f} \mu_t}{Pr_t} \right) \frac{\partial T}{\partial x_j} \right), \quad (8)$$

where  $\mu_t$  is eddy viscosity, which is expressed as

$$\mu_t = \frac{C_\mu \rho_f k^2}{\varepsilon}. \quad (9)$$

The kinetic energy and the dissipation energy equations are given, respectively, by

$$\rho_f U_j \frac{\partial k}{\partial x_j} = \frac{\partial}{\partial x_j} \left( \left( k_f + \frac{\mu_t}{\sigma_k} \right) \frac{\partial k}{\partial x_j} \right) + G - \rho_f \varepsilon \quad (10)$$

and

$$\rho_f U_j \frac{\partial \varepsilon}{\partial x_j} = \frac{\partial}{\partial x_j} \left( \left( k_f + \frac{\mu_t}{\sigma_\varepsilon} \right) \frac{\partial \varepsilon}{\partial x_j} \right) + C_1 G \frac{\varepsilon}{k} - C_2 \rho_f \frac{\varepsilon^2}{k}. \quad (11)$$

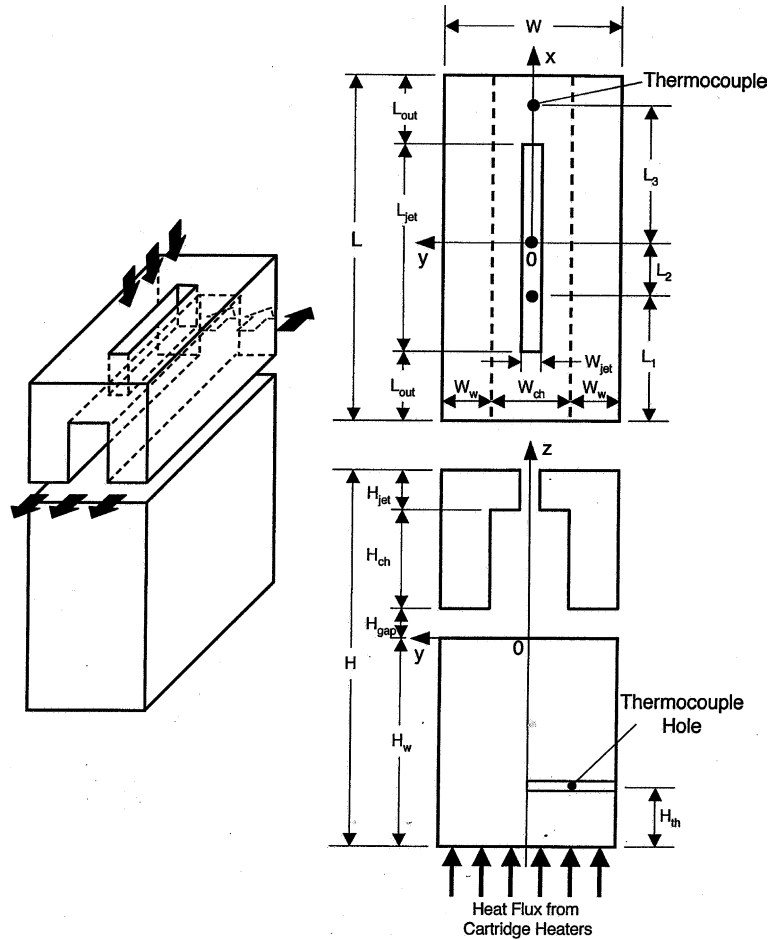


Fig. 4. Schematic of unit cell consisting of single jet and single channel.

Table 1  
Dimensions of unit cell of flow distribution plate

$L$ (mm)	$L_1$ (mm)	$L_2$ (mm)	$L_3$ (mm)	$L_{out}$ (mm)	$L_{jet}$ (mm)	$W$ (mm)	$W_{jet}$ (mm)
20.00	5.00	5.00	7.50	3.65	12.70	2.10	0.48
$W_{ch}$ (mm)	$W_w$ (mm)	$H$ (mm)	$H_{jet}$ (mm)	$H_{ch}$ (mm)	$H_{gap}$ (mm)	$H_w$ (mm)	$H_{th}$ (mm)
1.59	0.26	7.15	0.76	1.02	0.76	4.62	0.52

The production of turbulent energy is defined as  $G = -\overline{u_i u_j} \partial U_i / \partial x_j$ . As described by Launder and Spalding [18], the following values are used for the coefficients in the above equations:  $C_\mu = 0.09$ ,  $C_1 = 1.44$ ,  $C_2 = 1.92$ ,  $\sigma_k = 1.0$ , and  $\sigma_\epsilon = 1.3$ .

From analysis of experimental velocity and temperature profiles in a flat duct, Kays [20] concluded that for fluids with  $Pr > 0.5$ , the turbulent Prandtl number is a constant at about  $Pr_t = 0.85$  in the region where both profiles are logarithmic.

For the solid region of the computational domain, the continuity and momentum equations are simply

$$U_i = 0 \tag{12}$$

and

$$\frac{\partial}{\partial x_j} \left( k_s \frac{\partial T}{\partial x_j} \right) = 0. \tag{13}$$

A numerical method to solving this conjugate heat transfer problem is to treat the solid and fluid as a unitary computational domain and solve the above governing equations simultaneously [21]. The boundary conditions were specified as follows.

Velocity and liquid temperature at the jet inlet were assumed uniform and set equal to the values measured at the jet inlet.

$$u = 0, \quad v = 0, \quad w = -w_{in}, \quad \text{and} \quad T = T_{in} \quad \text{for} \quad 0 \leq x \leq L_{jet}/2, \\ 0 \leq y \leq W_{jet}/2, \quad \text{and} \quad z = H_{gap} + H_{ch} + H_{jet}. \tag{14}$$

The flow was assumed hydraulically and thermally fully developed at the outlet except the  $u$ -velocity component. Conserving mass over the computational domain, the outlet conditions are given by

$$\dot{m} = \dot{m}_{\text{in}}, \quad \frac{\partial v}{\partial x} = 0, \quad \frac{\partial w}{\partial x} = 0, \quad \text{and} \quad \frac{\partial T}{\partial x} = 0, \quad \text{for } x = L/2. \quad (15)$$

For the solid regions, a constant heat flux was applied along the copper bottom boundary of the unit cell.

$$-k_s \frac{\partial T}{\partial z} = q''_{\text{eff}}, \quad \text{for } 0 \leq x \leq L/2, \quad 0 \leq y \leq W/2, \quad \text{and } z = -H_w, \quad (16)$$

where  $q''_{\text{eff}}$  was set equal to the measured electrical power,

$$q''_{\text{eff}} = \frac{P_w}{A_t}. \quad (17)$$

The law of wall was used to examine the viscous sublayer or turbulent region near walls. The near-wall flow was assumed laminar where  $y^+ < 11.63$ . For  $y^+ > 11.63$ , the flow was considered turbulent and the wall function approach was used [22].

The finite volume method (FVM) technique was used to discretize the governing equations along the three spatial coordinates. The SIMPLER algorithm by Patanker [23] was used to couple velocities and pressure on staggered grids. A special numerical technique with a large source term was used to yield zero velocity in the solid region to facilitate solving the momentum and energy equations simultaneously. The discretized equations were solved iteratively using the tri-diagonal matrix algorithm line solver. The solution was deemed convergent when the criterion of  $\max|(\phi^{l+1} - \phi^l)/\phi^{l+1}| \leq 10^{-5}$  was satisfied, where  $\phi$  represents any dependent variable, namely  $u$ ,  $v$ ,  $w$ , or  $T$ , and  $l$  iteration number.

The grid system consisted of  $92 \times 62 \times 107$  nodes in the  $x$ ,  $y$ , and  $z$  directions, respectively. Three different grid systems,  $112 \times 77 \times 152$ ,  $92 \times 62 \times 107$ , and  $72 \times 47 \times 77$ , were first tested to check the sensitivity of the numerical results to mesh size. The temperature differences were less than 2.2% for the finer two grid systems. The second grid system,  $92 \times 62 \times 107$ , was therefore employed to reduce computation time and computer memory requirements. This grid was non-uniform, having a larger number of grid points near the wall and the inlet to better resolve the wall boundaries and developing region.

#### 4. Comparison of numerical predictions with experimental results

The primary purpose of the present experimental study was to assess the accuracy of the numerical model. Once validated, the numerical model becomes an effective tool for optimizing the geometry of the hybrid cooling scheme.

Fig. 5 compares the numerical results for temperature distribution along the thermocouple line (see Fig. 4)

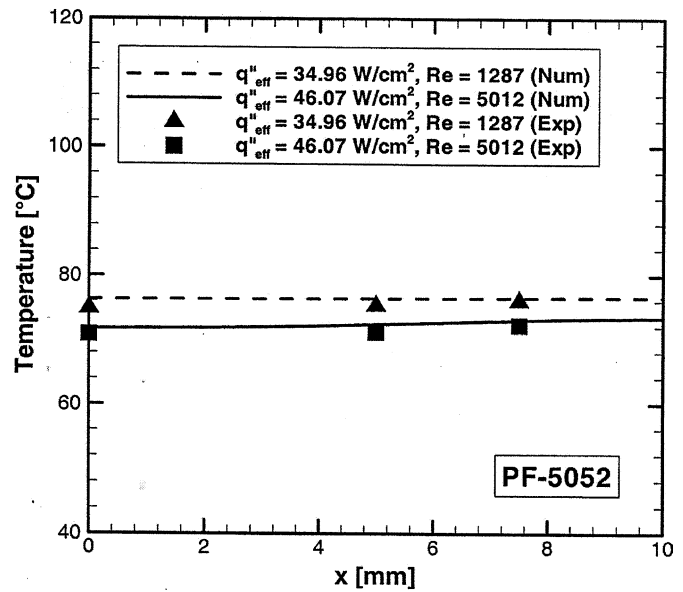


Fig. 5. Comparison of numerical predictions for temperature distribution along thermocouple line with experimental data.

against the thermocouple measurements for two heat fluxes and two Reynolds numbers. As expected, temperature increases along the flow direction. Based on the experimental results, increases in jet velocity increase the heat transfer coefficient and decrease the temperature gradient along the heater surface. More importantly, the excellent agreement between the predicted and measured temperatures shows the conventional Navier–Stokes and energy equations with the standard  $k$ – $\epsilon$  model can accurately predict heat transfer characteristics for the small flow passages of the present hybrid scheme. This is consistent with Qu and Mudawar's conclusion concerning micro-channel heat sinks [14].

Having validated the numerical methods, a more detailed depiction of the heat transfer characteristics of the test surface is now presented. The temperature distribution along the test surface of the unit cell is illustrated in Fig. 6(a) and (b) for  $q''_{\text{eff}} = 36.96 \text{ W/cm}^2$  with  $Re = 1287$  and  $q''_{\text{eff}} = 46.07 \text{ W/cm}^2$  with  $Re = 5012$ , respectively. For both cases, the surface temperature generally increases along the  $x$  direction, especially near the outlet. The lowest temperature is located along the centerline of the jet. Comparing Fig. 6(a) and (b) shows lower surface temperatures are achieved with the higher Reynolds number. A noteworthy trend is the minimum surface temperature is encountered below the center of the jet ( $x = 0$ ) for the lower Reynolds number but farther downstream for the higher Reynolds number. This trend may be explained by the increased flow blockage effects near the center of the jet with increasing Reynolds number.

Fig. 7(a) and (b) show velocity vectors and streamlines at  $x = 0.0 \text{ mm}$  for  $Re = 1287$  and  $5012$ , respectively. The impinging jet creates a stagnation zone immediately below, followed a recirculation pattern that is Reynolds number dependent. A higher jet velocity causes the jet fluid to reach

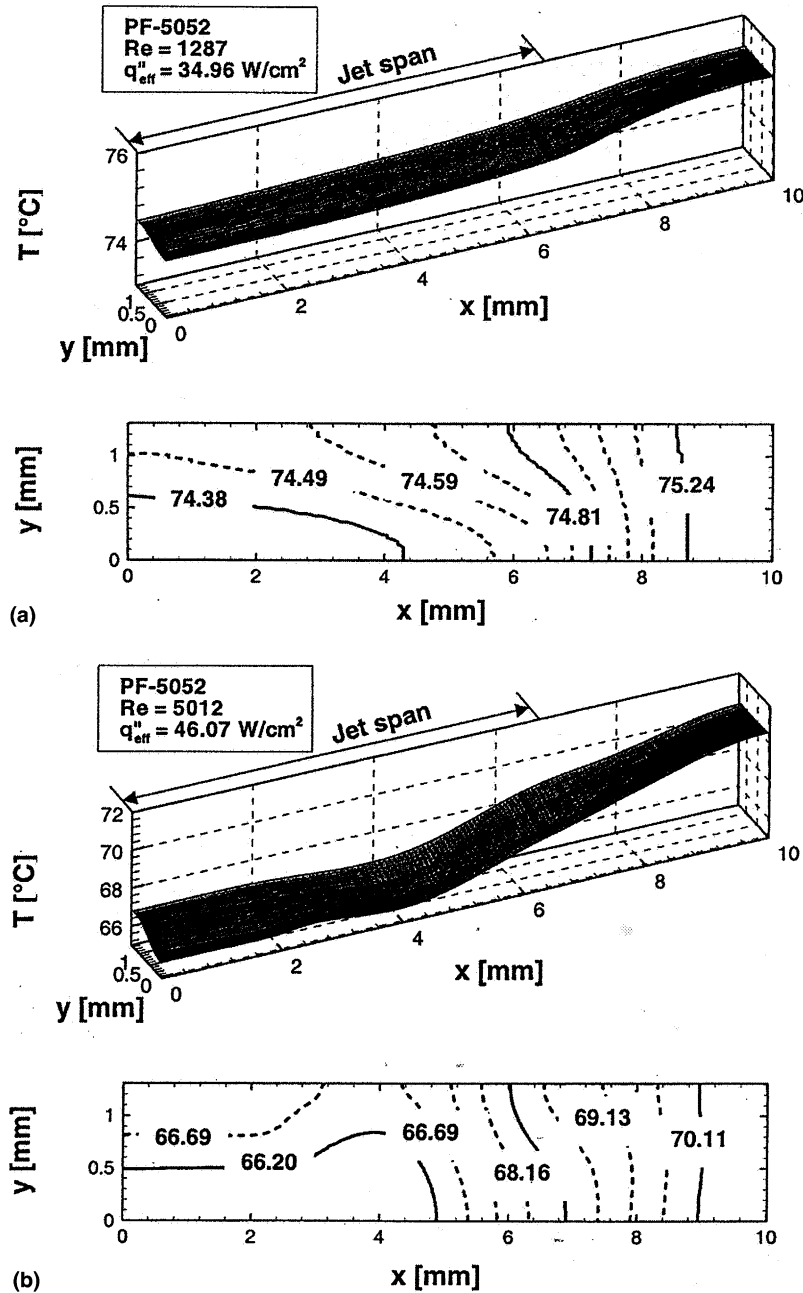


Fig. 6. Numerical predictions for test surface temperature distribution for (a)  $q''_{eff} = 34.96 \text{ W/cm}^2$  and  $Re = 1287$ , and (b)  $q''_{eff} = 46.07 \text{ W/cm}^2$  and  $Re = 5012$ .

closer to the test surface, producing the aforementioned decrease in the surface temperature. However, as shown in Fig. 6(b), a higher jet velocity causes appreciable acceleration of fluid along the surface, producing a surface temperature minimum downstream instead of at  $x = 0$ . Due to weaker attachment of the fluid to the test surface at the lower velocity, the jet fluid can more effectively occupy the upper regions of the flow area, producing far less acceleration along the surface, evidenced by a more uniform surface temperature below the entire jet as shown in Fig. 6(a).

Fig. 8(a) and (b) show the heat flux distribution along the heated surface, where the local heat flux is defined as

$$q'' = -k_s \left. \frac{\partial T_s}{\partial n} \right|_r \quad (18)$$

Both figures show higher heat fluxes are encountered along the centerline of the jet, i.e. at  $y = 0$ . The heat flux approaches zero outside the width of the jet. However, the heat flux in this same region increases downstream for the higher Reynolds number, Fig. 8(b), because of the aforementioned fluid acceleration in the  $x$  direction. As shown in Fig. 7(b), stronger attachment of the jet fluid to the surface pushes the high velocity liquid sideways to more effectively occupy the gap ( $H_{gap}$ ) region of the channel,

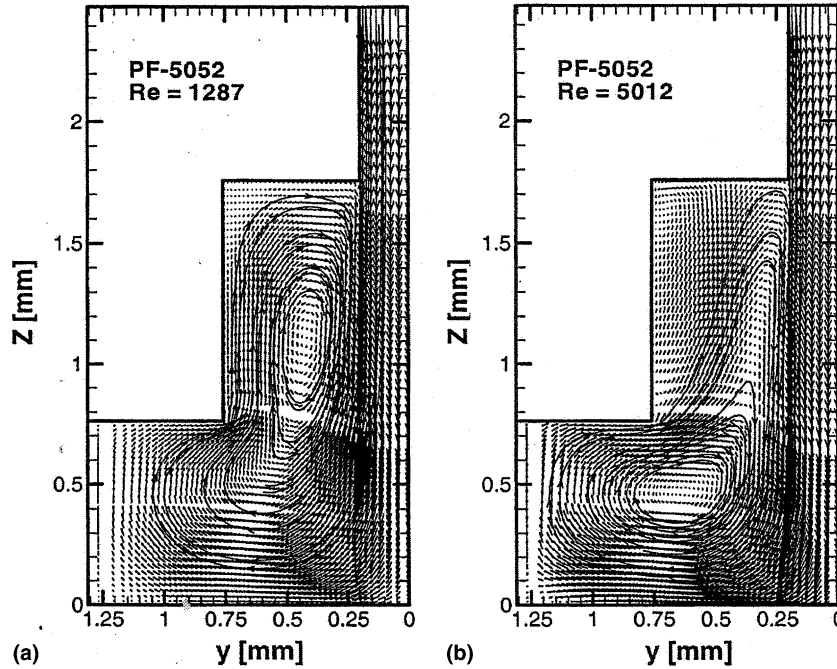


Fig. 7. Flow fields velocity at  $x = 0.0$  mm for (a)  $Re = 1287$  and (b)  $Re = 5012$ .

increasing the heat transfer coefficient in this side region as well.

Fig. 9(a) and (b) show similar heat transfer trends along the test surface for the local Nusselt number, which is expressed as

$$Nu = \frac{q'' d_h}{k_f (T_{s,f} - T_{in})} \quad (19)$$

A useful measure of the effectiveness of the hybrid cooling scheme is the  $x$ -direction variation of surface temperature averaged over the width,  $W$ , of the unit cell. This temperature can be evaluated from

$$T_{av}(x) = \frac{1}{W} \int_0^W T_{s,f} dy \quad \text{for } z = 0. \quad (20)$$

Similarly, the average heat flux and average Nusselt number are expressed, respectively, as

$$q''_{av} = \frac{1}{W} \int_0^W q'' dy \quad (21)$$

and

$$Nu_{av} = \frac{1}{W} \int_0^W Nu dy, \quad \text{for } z = 0. \quad (22)$$

Fig. 10(a)–(c) show variations of the average surface temperature, average heat flux and average Nusselt number, respectively, along the  $x$ -direction. Notice the average heat flux and the average Nusselt number are largest below the jet and decrease sharply towards the exit. The distributions for these parameters are far more complex for the higher Reynolds number because of the aforementioned acceleration effects. These effects produce local maxima in both parameters below the jet but downstream from  $x = 0$ .

### 5. Effects of flow distribution plate geometry

Large temperatures and spatial temperature gradients in modern devices constitute two key obstacles to the implementation of many seemingly effective cooling schemes for high-flux heat removal [1]. In this study, the effects of inlet liquid velocity and flow geometry on both maximum surface temperature and spatial temperature variations were investigated in pursuit of optimal dimensions for the flow distribution plate. To generalize the findings of this study to other coolants and high-flux applications, water was used as working fluid. Referring to Fig. 4, the optimization study explored the effects of four key parameters: jet width ( $W_{jet}$ ), gap height ( $H_{gap}$ ), and channel height ( $H_{ch}$ ). The inlet flow temperature and Reynolds number were set at 26.9 °C and 1921, respectively, using water as working fluid, and the entire bottom surface was subjected to constant heat flux of 125.21 W/cm<sup>2</sup>. Jet height ( $H_{jet}$ ) and channel width ( $W_{ch}$ ) were held constant in this parametric study. Values of the geometrical parameters examined are given in Table 2.

As shown in Fig. 11(a), the numerical simulation results reveal an advantageous decrease in the maximum temperature of the test surface with decreasing jet width. This is because the heat transfer coefficient is strongly dependent on jet velocity for a constant Reynolds number. However, this decrease in maximum surface temperature is realized with an increasing temperature gradient across the surface because of the smaller stagnation zone associated with a smaller jet width.

Fig. 11(b) shows the effects of gap height ( $H_{gap}$ ) on surface temperature for a jet width of  $W_{jet} = 0.25$  mm and a channel height of  $H_{ch} = 1.02$  mm. Reducing gap height is

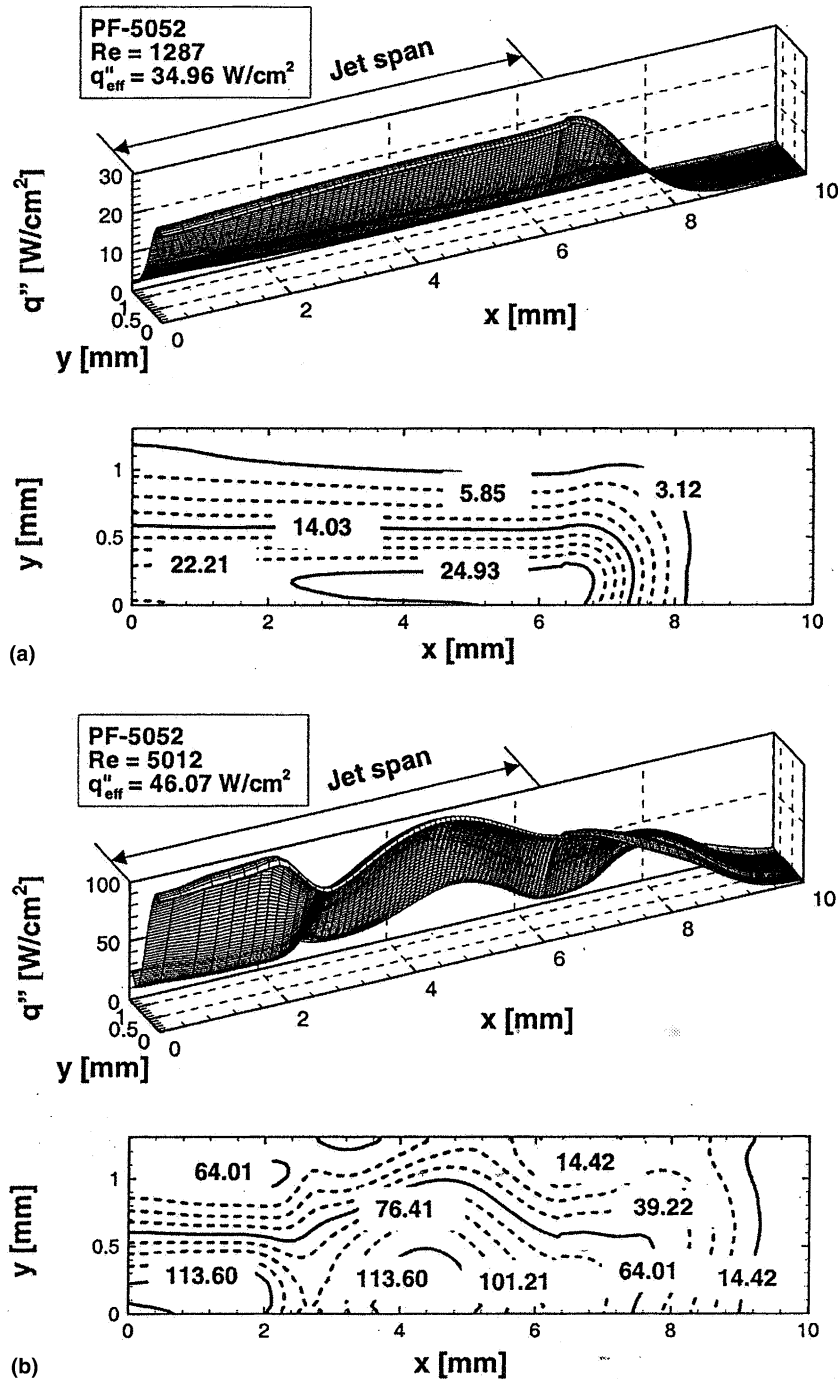


Fig. 8. Numerical predictions for test surface heat flux distribution for (a)  $q''_{\text{eff}} = 34.96 \text{ W/cm}^2$  and  $Re = 1287$ , and (b)  $q''_{\text{eff}} = 46.07 \text{ W/cm}^2$  and  $Re = 5012$ .

shown reducing both the maximum surface temperature and the temperature gradient across the surface, apparently due to the aforementioned fluid acceleration effects. The effect of gap height appears to weaken significantly for  $H_{\text{gap}} > 0.50 \text{ mm}$ .

Fig. 11(c) shows the effects of channel height ( $H_{\text{ch}}$ ) for a jet width of  $W_{\text{jet}} = 0.25 \text{ mm}$  and a gap height of  $H_{\text{gap}} = 0.25 \text{ mm}$ . Here too, decreasing channel height appears to decrease the maximum surface temperature; this effect appears to subside appreciably for  $H_{\text{ch}} > 0.80 \text{ mm}$ . The key

advantage of a smaller channel height is fluid acceleration along the test surface. This effect is greatly weakened for large channel heights because fluid streamlines maintain close proximity to the heated surface. Notice in Fig. 11(c) that channel height has an insignificant effect on the surface temperature gradient.

Fig. 12 shows how the hybrid cooling scheme can be configured to capitalize upon the aforementioned parametric trend in pursuit of (1) higher heat transfer coefficients (i.e. lower surface temperatures) and (2) lower temperature

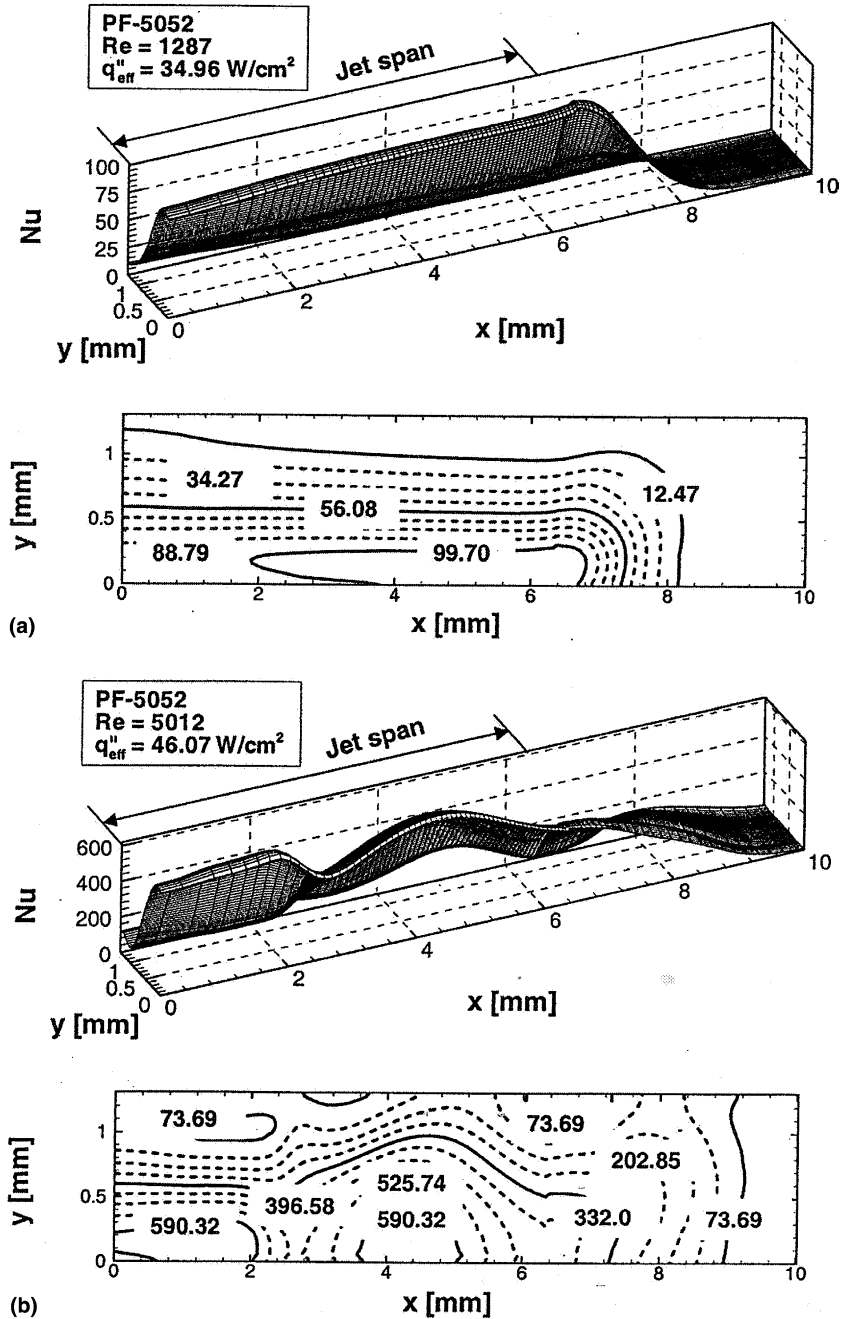


Fig. 9. Numerical predictions for test surface Nusselt number distribution for (a)  $q''_{eff} = 34.96 \text{ W/cm}^2$  and  $Re = 1287$ , and (b)  $q''_{eff} = 46.07 \text{ W/cm}^2$  and  $Re = 5012$ .

gradients across the surface. The channel used in the original design was intended to provide better flow control beneath each jet. However, the parametric results from Fig. 11 prove reducing both gap height and channel height will yield better results. In the limit, this can be accomplished by removing the channel feature of the hybrid cooling scheme (i.e. by setting  $H_{ch} = 0$ ), greatly simplifying the cooling geometry. The lower limit to gap height is dictated by the maximum pressure drop that may be tolerated by the flow loop supporting the cooling module. The preferred jet width is less straightforward. As indicated in Fig. 11, a smaller width can reduce surface temperature appreciably

because better cooling is possible by increasing jet velocity for a given Reynolds number. However, this may also increase the temperature gradient across the surface. The lower limit to jet width is therefore dictated either by the maximum temperature gradient that can be tolerated by the cooled device, or by pressure drop across the jet.

### 6. Conclusions

The fluid flow and heat transfer characteristics of a new hybrid jet-impingement/micro-channel cooling device were investigated both experimentally and numerically. The

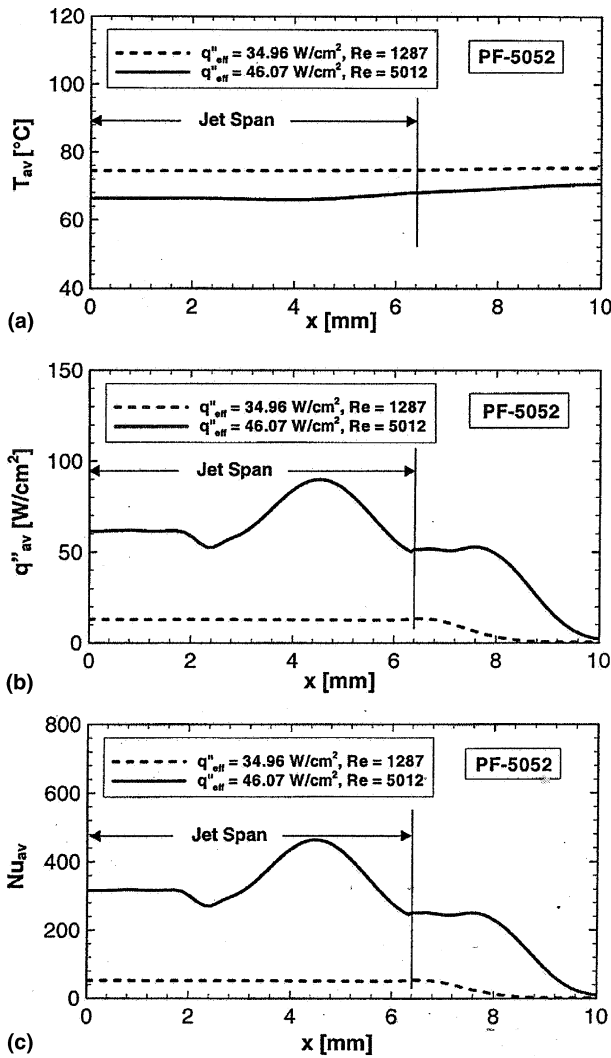


Fig. 10. Numerical predictions of average heat transfer characteristics along  $x$ -direction for (a) average temperature, (b) average heat flux, and (c) average Nusselt number.

Table 2  
Dimensions used in numerical optimization study

$L_{jet}$ (mm)	$W_{ch}$ (mm)	$H_{ch}$ (mm)	$W_{jet}$ (mm)	$H_{gap}$ (mm)
12.70	1.59	1.02	0.48	0.76
		0.76	0.25	0.51
		0.51	0.13	0.25
			0.06	

accuracy of a numerical model of the flow distribution plate for this scheme was first assessed against experimental data for PF-5052. The model was then used to both explore the local heat transfer characteristics of this cooling scheme and to optimize cooling performance for a water-cooled device. Key findings from the study are as follows:

1. Numerical predictions based on the standard  $k-\epsilon$  turbulence model show excellent agreement with measured heater block temperatures. This proves that, using this turbulence model, the conventional Navier–Stokes and

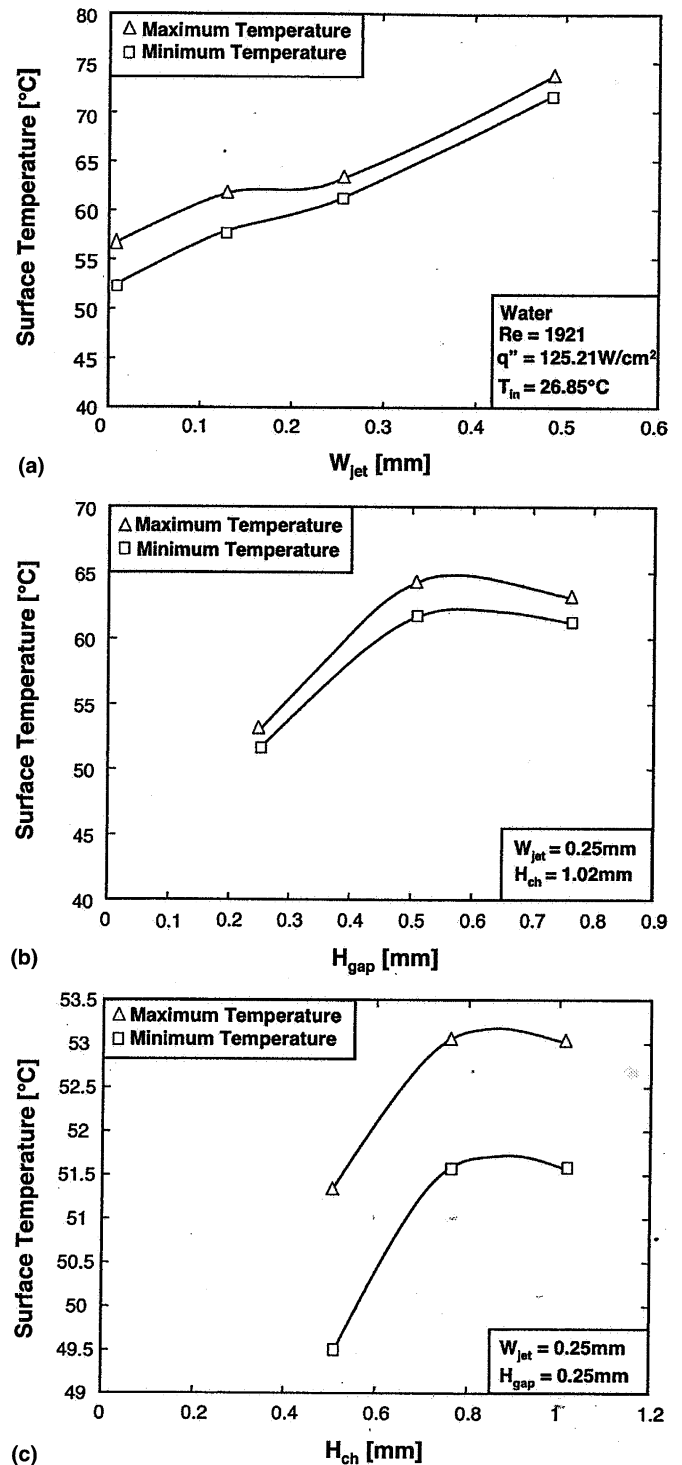


Fig. 11. Variation of test surface temperature with (a) jet width, (b) gap height, and (c) channel height for water.

energy equations can accurately predict the heat transfer characteristics for the small flow passages of the present hybrid scheme.

2. Vorticity has a great influence on fluid flow outside the impingement zone. Higher jet Reynolds numbers produce stronger fluid attachment to the heated surface and better utilization of the side gap region of the flow cross-section.

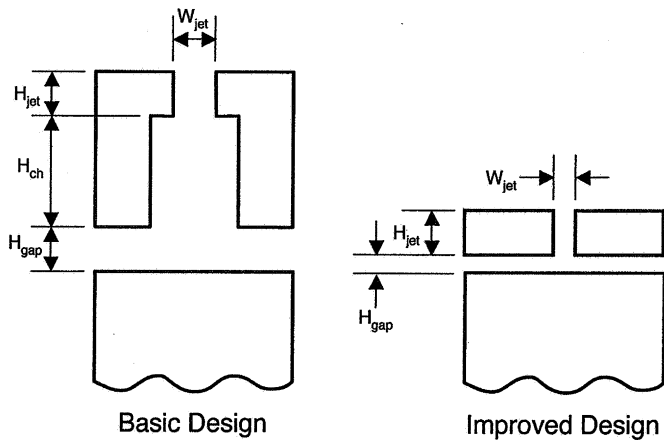


Fig. 12. Improvement of hybrid system design based on findings of optimization study.

3. For PF-5052, the surface temperature is generally lowest along the centerline of the jet and increases along the direction of fluid flow, especially near the outlet. Fluid acceleration at higher Reynolds numbers both lowers surface temperatures and yields a surface temperature minimum farther downstream from the center of the flow distribution plate.
4. Using water as working fluid, the numerical simulation results reveal an advantageous decrease in the maximum temperature of the test surface with decreases in jet width, channel height, and/or gap height. Decreasing channel height and gap height also serve to decrease the temperature gradient across the surface; decreasing jet width produces the opposite effect. The key advantage of smaller channel and gap heights is fluid acceleration along the test surface. The effects of channel height and gap height become far weaker above 0.80 and 0.50 mm, respectively.
5. Using numerical results for water, a simplified hybrid cooling geometry is recommended in pursuit of lower surface temperatures and smaller gradients across the surface. In the simplified design, the channel feature of the flow distribution plate is completely removed and the gap height greatly reduced to a level that is dictated largely by the pressure drop capability of the flow loop supporting the cooling module. Better cooling can also be achieved by decreasing jet width. However, a lower limit to jet width is dictated either by the maximum temperature gradient that can be tolerated by the cooled device, or by pressure drop across the jet.

#### Acknowledgement

The authors are grateful for the support of the Office of Naval Research (ONR) for this research.

#### References

- [1] I. Mudawar, Assessment of high-heat-flux thermal management schemes, *IEEE Trans. Compon. Pack. Technol.* 24 (2001) 122–141.
- [2] D.C. Wadsworth, I. Mudawar, Cooling of a multichip electronic module by means of confined two-dimensional jets of dielectric liquid, *ASME J. Heat Transfer* 112 (1990) 891–898.
- [3] K.A. Estes, I. Mudawar, Comparison of two-phase electronic cooling using free jets and sprays, *ASME J. Electron. Pack.* 117 (1995) 323–332.
- [4] H. Martin, Heat and mass transfer between impinging gas jets and solid surfaces, *Adv. Heat Transfer* 13 (1977) 1–60.
- [5] L.M. Jiji, Z. Dagan, Experimental investigation of single phase multi-jet impingement cooling of array of microelectronic heat sources, in: *Proc. Int. Symp. on Cooling Technology for Electronic Equipment*, Honolulu, HI, 1987, pp. 265–283.
- [6] S.J. Downs, E.H. James, Jet impingement heat transfer—a literature survey, ASME paper No. 87-Ht-35, 1987, ASME, New York, NY.
- [7] R.J. Goldstein, J.F. Timmer, Visualization of heat transfer from arrays of impinging jets, *Int. J. Heat Mass Transfer* 25 (1982) 1857–1868.
- [8] T.J. Craft, L.J.W. Graham, B.E. Launder, Impinging jet studies for turbulence model assessment—II. An examination of the performance of four turbulence models, *Int. J. Heat Mass Transfer* 36 (1993) 2685–2697.
- [9] T.H. Park, H.G. Choi, J.Y. Yoo, S.J. Kim, Streamline upwind numerical simulation of two-dimensional confined impinging slot jets, *Int. J. Heat Mass Transfer* 46 (2003) 251–262.
- [10] E. Baydar, Y. Ozmen, An experimental and numerical investigation on a confined impinging air jet at high Reynolds numbers, *Appl. Therm. Eng.* 25 (2005) 409–421.
- [11] D.B. Tuckerman, R.F.W. Pease, High-performance heat sinking for VLSI, *IEEE Electron. Dev. Lett.* EDL-2 (1981) 126–129.
- [12] A. Weisberg, H.H. Bau, J.N. Zemel, Analysis of microchannels for integrated cooling, *Int. J. Heat Mass Transfer* 35 (1992) 2465–2474.
- [13] A.G. Fedorov, R. Viskanta, Three-dimensional conjugate heat transfer in the microchannel heat sink for electronic packaging, *Int. J. Heat Mass Transfer* 43 (2000) 399–415.
- [14] W. Qu, I. Mudawar, Experimental and numerical study of pressure drop and heat transfer in a single-phase micro-channel heat sink, *Int. J. Heat Mass Transfer* 45 (2002) 2549–2565.
- [15] S.J. Kim, D. Kim, Forced convection in microstructures for electronic equipment cooling, *ASME J. Heat Transfer* 121 (1999) 639–645.
- [16] E.Y.K. Ng, S.T. Tan, Computation of three-dimensional developing pressure-driven liquid flow in a microchannel with EDL effect, *Numer. Heat Transfer A* 45 (2004) 1013–1027.
- [17] K.K. Ambatipudi, M.M. Rahman, Analysis of conjugate heat transfer in microchannel heat sinks, *Numer. Heat Transfer A* 37 (2000) 711–731.
- [18] B.E. Launder, D.B. Spalding, The numerical computation of turbulent flows, *Comput. Methods Appl. Mech. Eng.* 3 (1974) 269–289.
- [19] F.H. Harlow, J.E. Welch, Numerical calculation of time-dependent viscous incompressible flow of fluid with free surface, *Phys. Fluids* 8 (1965) 2182–2189.
- [20] W.M. Kays, Turbulent Prandtl number—Where are we? *ASME J. Heat Transfer* 116 (1994) 284–295.
- [21] S.V. Patankar, A numerical method for conduction in composite materials, flow in irregular geometries and conjugate heat transfer, in: *Proc. Third Int. Heat Trans. Conf.*, Toronto, Canada, vol. 3, 1978, pp. 297–302.
- [22] H.K. Versteeg, W. Malalasekera, *An Introduction to Computational Fluid Dynamics, The Finite Volume Method*, Wiley, New York, NY, 1995.
- [23] S.V. Patankar, *Numerical Heat Transfer and Fluid Flow*, Hemisphere, Washington, DC, 1980.